Nanoscale

PAPER

View Article Online
View Journal

Cite this: DOI: 10.1039/d5nr03470a

Exploring the structural conditions favoring Au anionic behavior on Au doped CeO_2

L. E. López-González, * R. Ponce-Pérez, Sergio A. Aguila, Mario H. Farías, T. A. Zepeda-Partida, F. F. Castillon-Barraza* and J. Guerrero-Sanchez *

In this work, we conducted a systematic study of the synthesis and structural and chemical characterization of Au-doped CeO_2 materials to identify the conditions under which the anionic character of gold is observed, using both experimental and density functional theory simulations. Successful incorporation of Au into the samples was detected from infrared spectra and X-ray diffraction analysis. As the Au concentration increased, an increase in defects and a reductive chemical environment was observed using UV-vis spectra. The presence of Au loading onto CeO_2 as particles in the high Au concentration samples was determined with SEM images and EDS spectra. The Au adsorption on the CeO_2 (111) surface was found to be the most stable by means of DFT modeling. The most stable Au adsorption models incorporated an oxygen vacancy and Au substituting an oxygen atom. Further Bader charge analysis revealed that Au had a negative character in these models. X-ray induced photoelectron spectra uncovered that in the low mol% concentration regime, there is a presence of anionic Au behavior. Further high-resolution window chemical species quantification and correlation confirmed that anionic character was promoted by Au substituting oxygen atoms as pointed out by DFT calculations, implying that anionic gold was present and has indeed previously not been contemplated in Au-doped CeO_2 applications.

Received 16th August 2025,
Accepted 29th March 2026

DOI: 10.1039/d5nr03470a

rsc.li/nanoscale

Introduction

The global growth in energy consumption has driven the excessive use of non-renewable energy sources, primarily fossil fuels, which has drastically increased atmospheric pollution.[1,2] One of the toxic byproducts is carbon monoxide (CO), which is known to block oxygen absorption in blood, causing severe health problems and a cascade of ecological impacts,[3] which pushes research to the point of developing strategies to diminish these impacts and phase out no-return consequences. One of the main tactics to reduce CO in the atmosphere is to induce its oxidation to CO_2 using catalytic conversion.[2]

The primary approach for designing materials for this purpose is to utilize a platform that promotes oxidation by altering the oxidation state of a metal in a compound. In this context, CeO_2 is a notable platform for this process, mainly because of its ability to store and release a large amount of oxygen through defect switching between different oxidation states, making it suitable for different types of oxidation reactions.[4] Ceria is well-known in the literature for its facile transition between reduced and oxidized states ($Ce^{3+} \leftrightarrow Ce^{4+}$) due to its rapid and reversible ability to uptake and release oxygen,[5,6] playing an essential role in three-way catalysts.[7] The dynamic oxygen storage capacity of ceria is related to the donation of available oxygen atoms; its high capacity is, among other causes, attributed to a relatively high amount of oxygen vacancies on its surfaces, playing a role in adsorption and activation of oxygen and also proving to be proportioned sites for adsorption and activation of reactant molecules.[4] A conjunction of the above-mentioned aspects of ceria makes it an advantageous support for oxidation reactions.

Similarly, due to their high activity, noble metals have proven to be effective catalysts for CO oxidation; thus, adding noble metals as dopants to oxide supports has resulted in even better catalysts. Apart from doping, the loading of noble metals has shown better catalytic efficiency than the pristine materials.[8]

Among noble metals, gold stands out as a versatile material with remarkable catalytic behavior, which is mainly attributed to the small particle size in metallic Au, due to a major presence of low coordinated Au atoms on the surface, with this species being responsible for adsorption of reactants. Other relevant factors are the likely high mobility of surface atoms on small particles and the electronegative character of gold, both of which arise from the relativistic contraction of the s-electron orbitals.[9] When used as a dopant, Au typically behaves as a cation, exhibiting oxidation states ranging from Au^{1+} to Au^{3+}. This gold species has also been linked to

Centro de Nanociencias y Nanotecnología, Universidad Nacional Autónoma de México, Ensenada, BC 22860, Mexico. E-mail: luis.lopez@ens.cnyn.unam.mx, fcastillon@ens.cnyn.unam.mx, guerrero@ens.cnyn.unam.mx

enhanced catalytic activity on Au doped CeO_2.[4] However, among the above-described particularities is the high electronegative character of gold, which, upon interaction with electropositive atoms such as alkaline and alkaline earth metals, can behave as an anion (with the oxidation state Au^-). A typical example of this gold species is CsAu;[10,11] however, it has also been found in other solid materials such as A_2MAu_6 perovskites,[12] organic gold complexes,[13] and also on the surface of metallic Au particles.[14] In this context, rare earth oxides such as CeO_2 exhibit the characteristic low electronegativity of their metal, making them a likely platform for encountering Au anionic species. Moreover, the structural and chemical conditions that induce anionic responses on CeO_2 and their impact on catalytic behavior in conjunction with other Au species (metallic and cationic) have not yet been studied; furthermore, the spectrum of possible applications has not been explored.

To identify the structural conditions that may induce an anionic behavior, we conducted an experimental and theoretical simulation study. The first part consisted of the synthesis, structural, and spectroscopic characterization of Au-modified CeO_2. The EDS spectra of the materials at varying Au concentrations revealed the effect of Au concentration on the structural properties of the rare-earth oxide. Infrared spectra and X-ray diffraction analysis showed the successful incorporation of Au into the samples. In the second part, we employed computational modeling and density functional theory (DFT) calculations to identify the conditions that induce anionic behavior of Au on CeO_2 surfaces. Au adsorption on the CeO_2 (111) surface revealed that the most stable Au adsorption models incorporated an oxygen vacancy and Au substituting an oxygen atom. Further Bader charge analysis revealed that Au had a negative character in these models. Finally, the chemical surface characterization and quantification correlation study by X-ray photoelectron spectroscopy (XPS) allowed us to experimentally confirm the presence of these anionic species, revealing that anionic character was promoted by Au substituting oxygen atoms as predicted by DFT calculations. These findings suggest that the presence of anionic gold has not been previously considered and could have an impact on the catalytic behavior of Au-modified CeO_2 materials.

Materials and methods

Synthesis of gold doped CeO_2

The materials employed in this work were synthesized following the methodology described by Mittal and coworkers, with modifications.[15] Initially, for pristine CeO_2, a 25 mL 0.3 M solution of cerium nitrate hexahydrate ($Ce(NO_3)_3{\cdot}6H_2O$) (Sigma Aldrich) was prepared, followed by the addition of 1.0% (at wt) thioglycerol (TG) (Sigma Aldrich) with continuous stirring for 30 min. To this solution, 0.3 M NaOH (Sigma Aldrich) was added dropwise until reaching pH 7.5, which initiated the formation of a colored suspension, which transformed to light-yellow after 30 min of stirring.

For the synthesis of Au-doped CeO_2 samples at low Au concentrations (0.1 mol%, 0.3 mol%, 0.4 mol%, and 0.5 mol%) and high Au concentrations (5 mol%, 10 mol% and 15 mol%) at pH 7.5, gold chloride ($AuCl_3$) (Sigma Aldrich) was dissolved in deionized water at each required concentration in a volume of 25 mL and then added to the 0.3 M solution of Ce $(NO_3)_3{\cdot}6H_2O$ before the addition of TG. The rest of the procedure followed was the same as for pristine samples.

The precipitated materials were filtered using Whatman-40 filter paper and were washed several times with deionized water to remove impurities. The wet powders were dried at 70 °C in an oven for 24 hours. Finally, the samples were calcined at 250 °C for 2.5 hours to remove residual organics, stabilize the CeO_2 support, and minimize Au nanoparticle sintering.

Sample characterization

The addition of Au to the CeO_2 lattice was determined using Fourier transform infrared spectroscopy (FT-IR). The transmittance spectra were recorded using a Bruker Tensor-27, with KBr (Sigma Aldrich) as the background material in pressed pellets (5 tons per 3 min). The crystallinity of the synthesized materials was determined by X-ray diffraction (XRD) analysis using a Philips X'pert MPD diffractometer using Cu $K_{\alpha I}$ (k = 1.54 Å) radiation at a scanning rate of 0.04° s^{-1}. The lattice parameters and grain sizes were determined by Rietveld refinement. The UV–vis diffuse reflectance spectroscopy (DRS) measurements were recorded using an Agilent Cary-5000 UV-Vis spectrophotometer equipped with an integrating sphere. Scanning electron microscopy (SEM) images were obtained to analyze morphology and to determine the presence and segregation of Au. A JEOL JIB-4500 focused ion beam scanning electron microscope (SEM/FIB – 15 kV – ×40000) was employed. Transmission electron microscopy (TEM) images were also obtained using a Hitachi H-7650 microscope. In addition, to determine the chemical composition and oxidation states of Au on the Au-doped CeO_2 materials on the surface, X-ray photoelectron spectroscopy (XPS) measurements were performed in a SPECS system equipped with a PHOIBOS WAL analyzer using an Al anode.

Density functional theory (DFT) calculations

We performed first-principles calculations based on the periodic density functional theory implemented in the Vienna *Ab initio* Simulation Package (VASP)[16–19] to investigate the structural conditions under which gold behaves as an anion. Electronic states were expanded in plane waves with an energy cutoff of 450 eV. The electron–ion interaction was treated employing the pseudopotential method with PAW pseudopotentials.[20] The exchange–correlation energies are calculated using the generalized gradient approximation (GGA) with PBE parametrization.[21] van der Waals interactions have been accounted for by employing the D3 correction method of Grimme *et al.*[22,23] The DFT + U correction was employed to describe correctly the Ce f electrons with a U value of 5 eV.[24] We used the supercell method to simulate gold-modified

cerium oxides in a 2 × 2 × 1 supercell, a size appropriate for the assessed Au content. In geometry optimization, convergence is achieved when all force components are less than 0.01 eV Å^{-1} and the energy differences are less than 1 × 10^{-4} eV, as reported in previous studies.[2] The Brillouin zone was sampled with an equally spaced *k*-point mesh in a 6 × 6 × 6 grid for the unit cell. A comparison of total density of states (TDOS) for bulk CeO_2 employing Gaussian and Methfessel–Paxton smearing was made (Fig. S1). No significant change in the TDOS and the band gap value was observed. A Methfessel–Paxton smearing[25] was used. In the SI (Fig. S2–4), we provide details on the computational parameter optimization considered in this work.

Since we are dealing with surface terminations of different atom numbers, we employ the surface formation energy formalism (SFE) to investigate the stability of structures.[26] The SFE was calculated using the following formula:

$$E_f = E_{slab} - E_{ref} - \Delta n_O \mu_O - \Delta n_{Ce} \mu_{Ce} - \Delta n_{Au} \mu_{Au}$$

where E_{slab} is the total energy of the system at hand, E_{ref} is the total energy of an arbitrary reference; in this case, the reference is the clean CeO_2(2 × 2) supercell, μ_i is the chemical potential of the i^{th} species, and Δn_i is the excess or deficit of the i^{th} species. The SFE is a function of the O chemical potential with a lower limit (O-rich conditions) $\mu_O = \mu_O^{molecule}$ and an upper limit (O-poor conditions) $\mu_O = \mu_O^{molecule} - \Delta H_f$, with ΔH_f being the bulk CeO_2 formation enthalpy. To determine the Ce ΔH_f, we employed the hexagonal phase with 4 atoms per unit cell. According to calculations, ΔH_f = 6.37 eV. μ_O and μ_{Au} are obtained by modeling the O_2 molecule in a 10 Å cube and the Au FCC phase with 4 atoms per unit cell, respectively.

Results and discussion

Effect of Au concentration on the structural properties of CeO_2

Based on the idea that gold in an anionic state would be favored by the CeO_2 surface defects and the low electronegativity of Ce atoms, the samples prepared for this work involved two Au concentration regimes, at low Au concentrations (from 0.1 to 0.5 mol%) and high concentrations (from 5 to 15 mol%), expecting an Au surface substitution effect to be favored at low concentrations and particle aggregates to form on the CeO_2 surface at high concentrations.

First, to confirm the Au integration into the CeO_2 lattice, FT-IR spectra were recorded for all the prepared samples. Results are presented in Fig. 1. The high concentration regime spectra for the functional group and the fingerprint region are shown in Fig. 1a and b, respectively. In the functional group region, the shift to higher wavenumber values on the O–H stretch (3314 cm^{-1} for pristine CeO_2) indicated that surface OH groups interact less, attributed to the less formation of ordered hydrogen bonds due to a more distorted lattice as the amount of gold increased. In the fingerprint region, the Ce–O stretch band was observed at 503 cm^{-1} for pristine CeO_2.[27] As the gold concentration increased, a shift to a lower wavenumber was observed, indicating that the Ce–O bond weakened with the addition of gold. The shift stopped after 5 mol% concentration, indicating bulk saturation and further gold particle aggregation.

For the low-concentration regime in the fingerprint region, a gradual shift of the Ce–O stretching band was also observed as the gold concentration increased, indicating gold incorporation into the CeO_2 lattice.

To confirm the crystallographic phases, samples were measured by powder XRD in the range of 20° to 80°. Results are presented in Fig. 2 for both sets of samples: the high concentration regime (Fig. 2a) and the low concentration regime (Fig. 2b). The two plots show the crystallographic chart for the CeO_2 FCC (ICSD 034-0394) and the Au FCC (ICSD 004-0784) as well as the corresponding diffractogram for each sample. Results validated the fluorite structure (FCC) of CeO_2 for all the samples. Additionally, the presence of gold in the FCC structure was confirmed in the three high-concentration regime samples by the appearance of the corresponding diffraction peaks, which were absent in the low-concentration regime samples. This result confirms the presence of doping at low concentrations and the coexistence of doping and particle segregation at high concentrations.

To have a clearer view of the effect of the Au concentration on the crystal structure of CeO_2, X-ray diffractograms were analyzed by Rietveld refinement to determine the lattice parameter. Plots of the measured lattice parameter as a function of the Au concentration were constructed. Fig. S5a shows that in the low concentration regime, as the Au concentration increases, the lattice parameter slightly decreases until the value of 0.5 mol%. For the high concentration regime (Fig. S5b), it initially diminished and then remained in a similar range. This decrease in lattice constant was consistent with the smaller ionic radius of Au ions (0.53 Å) than both Ce^{4+} (0.92 Å) and O^{2-} (1.38 Å). The observed behavior suggests that the addition of Au leads to significant changes in the electronic environment of CeO_2. The addition of gold atoms may induce an increase in defects, as well as a reduction in Ce atoms.

Furthermore, to gain insight into the effect of Au concentration on crystallite size, the Scherrer crystallite size was determined from Rietveld refinement results. These results are presented in Fig. S6. In the low concentration regime, the trend showed that as the Au concentration increased, the crystallite size gradually increased (Fig. S6a), suggesting that small amounts of gold may act as nucleation enhancers or crystal growth promoters. For the high concentration regime (Fig. S6b), as the Au concentration increased, the crystallite size decreased, indicating that excess Au begins to hinder grain growth.

Once we confirmed Au integration into the lattice samples, the electronic structure of the system was investigated by UV-Vis diffuse reflectance spectroscopy (DRS). The results are presented in Fig. 3. According to the literature, bands at 270 and 345 nm correspond to $Ce^{3+} \leftarrow O^-$ and $Ce^{4+} \leftarrow O^-$ charge transfer processes, respectively.[28] As the gold concentration

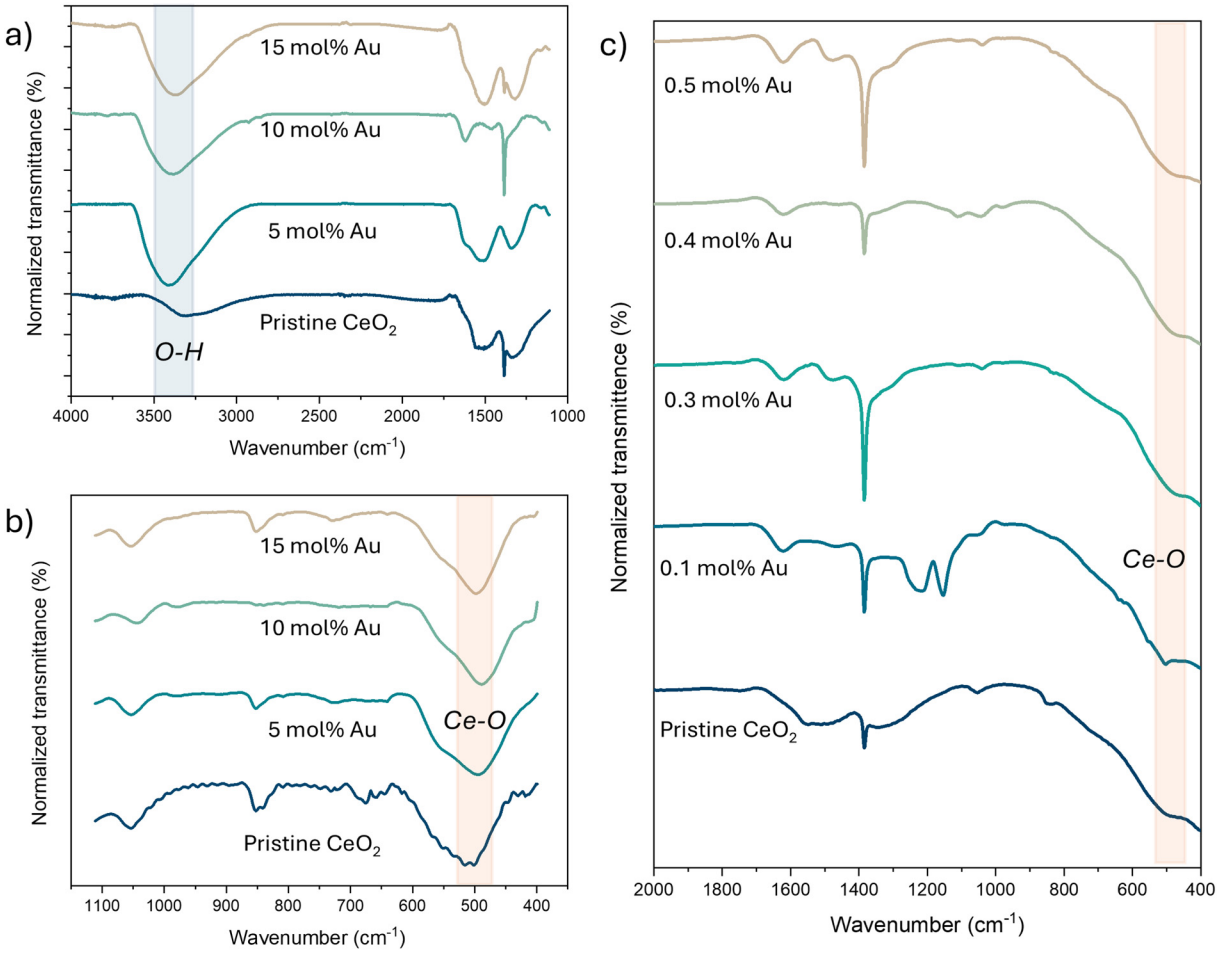

Fig. 1 Transmittance FT-IR spectra for the different synthesized cerium oxide materials at different concentrations of gold. (a) Functional group and (b) fingerprint region for the high Au concentration regime. (c) Fingerprint region for the low Au concentration regime.

increased, diminishing intensity was observed for the band corresponding to $Ce^{4+} \leftarrow O^{-}$ charge transfer, while the $Ce^{3+} \leftarrow O^{-}$ charge transfer increased. This behavior is more clearly illustrated in the inset plot of Fig. 3, which shows the band maxima as a function of gold concentration, and the intensity maximum corresponding to Ce^{4+} started to decrease after the initial concentration, while the one corresponding to Ce^{3+} remained constant after the first increase, indicating that as gold is incorporated into the CeO_2 lattice, an increase in defects and a reductive chemical environment is induced. In the range of 450–700 nm, a broad band appeared, which did not appear at the pristine CeO_2, corresponding to the surface plasmon resonance of the metallic Au nanoparticles and affected by the morphology of the gold particle and the dielectric properties of the chemical environment;[2,29] these bands also increase with increasing gold concentration, indicating an increase in the amount of segregated particles.

From XRD Rietveld refinement analysis, the segregated Au composition was estimated (Table S1), finding that the Au particle segregation amount increased with Au concentration, corresponding to the observed DRS UV-vis results.

Although UV-vis analysis indicated that a fraction of the material was nanostructured, SEM micrographs (Fig. S6) revealed a wide range of particle sizes, spanning from the micro to nanoscale, as well as diverse morphologies. These results were observed despite the varying Au concentration (Fig. S6a and b); however, in the high concentration regime, the back-scattered electron image enabled us to observe the segregated gold particles as intense, white contrast spots (Fig. S6c). The EDS spectra (top panels in Fig. S6) revealed the bulk sample's chemical elemental composition, indicating that Au was only detected in the high-concentration regime, giving additional support to the XRD results for the presence of the Au cubic phase in the high-concentration regime samples, further confirming the Au particle segregation.

Furthermore, to gain insight into the material morphology at the nanoscale, as well as Au particle segregation behavior, TEM images were collected; these results are presented in Fig. 4. In general terms, no specific morphology was observed. A homogeneous distribution of particle conglomerates that ranged from 50 to 200 nm was observed for pristine CeO_2 (Fig. 4a and b), and a similar morphology was observed for the

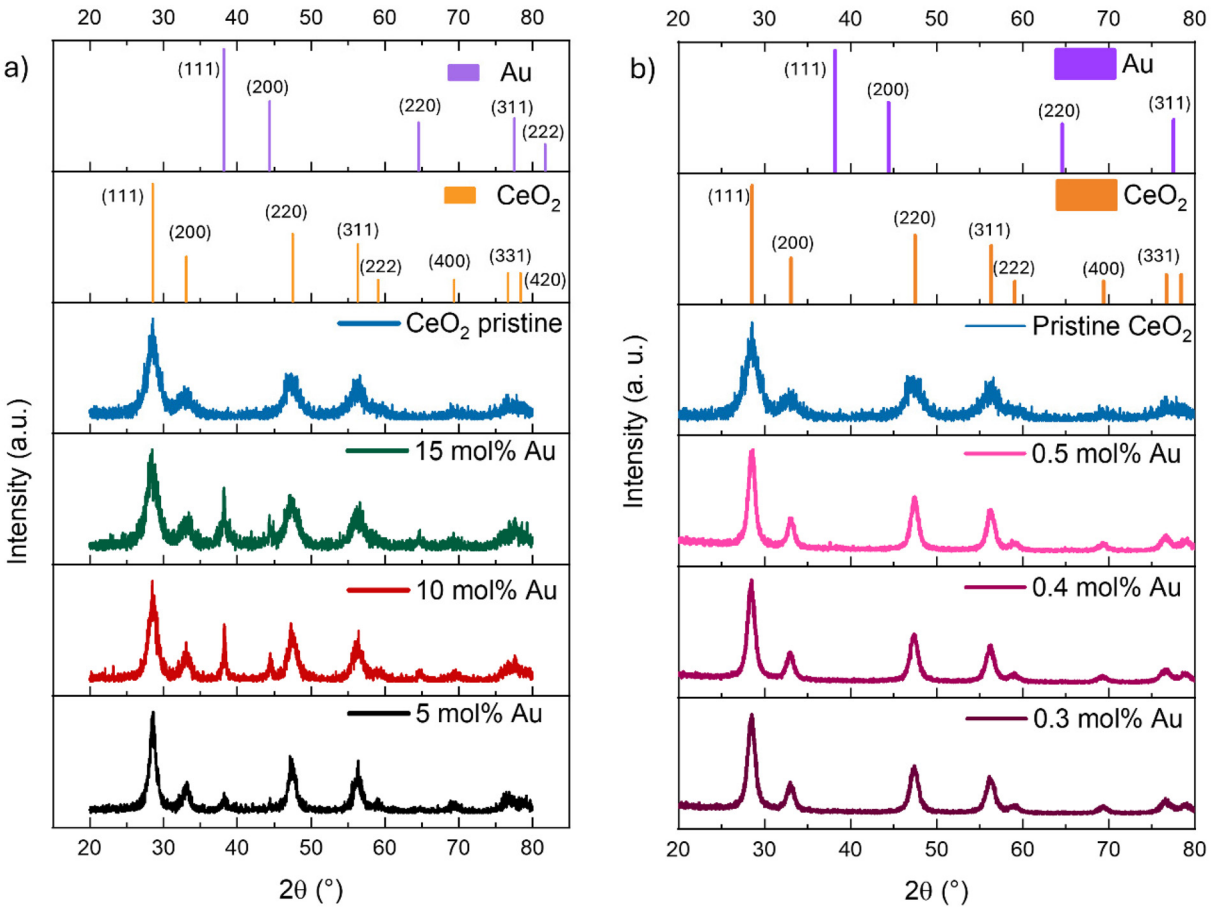

Fig. 2 Powder X-ray diffractograms for the different synthesized cerium oxide materials at different concentrations of gold (a) for the high Au concentration regime and (b) the low Au concentration regime.

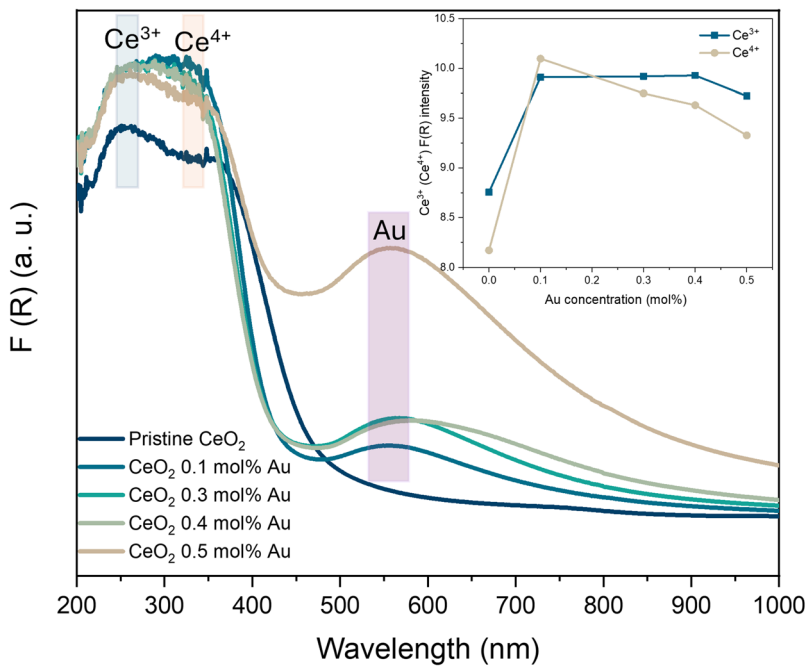

Fig. 3 Diffuse reflectance UV-vis spectra for the cerium oxide materials in the low Au concentration regime. The inset shows the evolution of the intensity of the Ce^{3+} and Ce^{4+} species with respect to Au concentration.

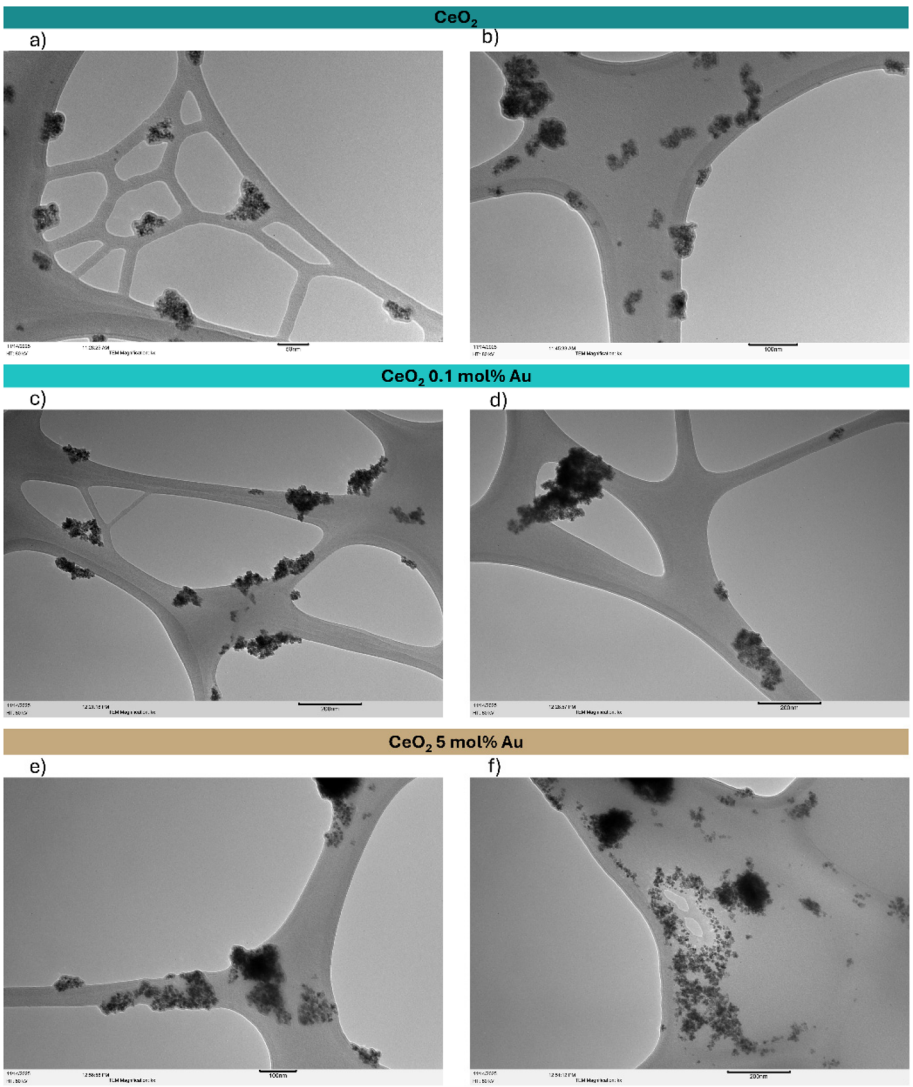

Fig. 4 TEM micrographs for (a, b) pristine CeO_2, (c, d) in the low Au concentration regime and (e, f) in the high concentration regime at two different magnifications.

low-concentration regime sample (Fig. 4c and d). For the high-concentration Au-doped CeO_2 sample (Fig. 4e and f), a different type of particle appeared, with a shape similar to the cubic shape; these formations were attributed to the segregated Au particles.

The UV-vis spectra indicated an increase in defects and a reductive chemical environment as the Au concentration increased; both conditions were further considered to model the system and, by *ab initio* calculations, determine the Au charge characteristics under different structural adsorption conditions. These results are discussed in the next section.

Au adsorption on the CeO_2 (111) surface: conditions to observe Au anionic behavior

A major critical point was to establish the conditions under which gold could present different electronic states. It is expected that a more reduced and defective environment on the CeO_2 surface would be a more likely surrounding for reducing Au atoms. According to the literature, vacancy formation energies on CeO_2 follow the order {1 1 0} < {1 0 0} < {1 1 1};[30] however, the most stable surface according to the literature is (111).[31] Hence, this work focused mainly on the simulation of the (111) surface and was complemented with a survey study of the adsorption of Au on the (110) surface. The pristine CeO_2 (111) surface was first constructed and then relaxed. After this, an oxygen vacancy (O-v) model was built and geometrically optimized.

Subsequently, the incorporation of Au was assessed. To determine the most likely binding sites of Au on CeO_2, electrostatic potential maps were plotted (Fig. S8). The results showed a negative potential for oxygen atoms and a positive potential for cerium, indicating that the most probable incorporation sites on both pristine and defective surfaces would be on top of O atoms and in tetrahedral sites between three Ce atoms.

The incorporation of Au was carried out in this manner in both cases, where Au, on the O-v model, was positioned on top of O and at the O-v site. Results for the obtained models and their surface stability assessment are presented in Fig. 5. The pristine surface models' adsorption structures (Fig. 5a and b) show practically no change in geometry with respect to the pristine CeO_2 (111) surface model (Fig. S9), whereas in the defective one, an apparent change in structure is observed in both models (Fig. 5c and d), the effect attributed to the O-v. The stability of the present models was analyzed using the SFE formalism, constructing plots of the SFE as a function of the chemical potential change of O atoms, with limits indicating poor and rich O conditions (Fig. 5e). Models were compared to the clean CeO_2 surface as a reference. Results showed that the most stable model in this comparison was the O-v with no Au adsorption, followed by the adsorption of Au on the O-v. Then the O on top adsorbed on the O-v model, while the Au adsorption in the pristine CeO_2 surface models was the least stable. This trend is consistent with experimental reports, which indicate that a highly O-v defective surface is the naturally occurring state of CeO_2.[32] Based on these results, we constructed adsorption models where, in addition to the O-v, an oxygen atom nearby to an oxygen vacancy was substituted with Au and compared the stability with respect to the oxygen depth of substitution. These results are summarized in Fig. 6. The three relaxed adsorption models are presented in Fig. 6a–c. Models show a significant geometry change after incorporating Au; the model presented in Fig. 6a reveals that the substitution of O closest to an O-v, Ce–O bond stress for the nearest neighbors to Au was observed, while the area corresponding to the

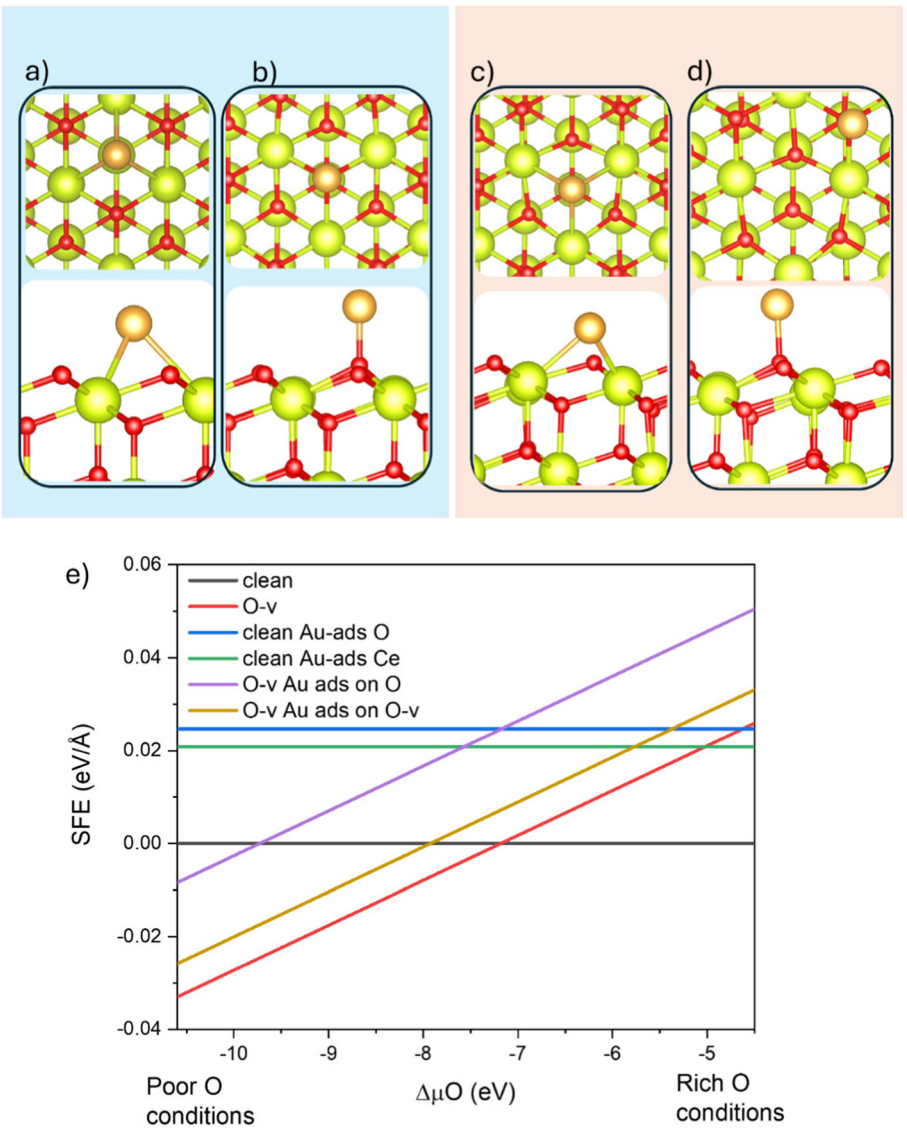

Fig. 5 Adsorption of Au on the CeO_2 (111) surface. Non-defective (blue panel), (a) at the Ce tetrahedral site and (b) on top of an O atom. O vacancy (red panel) (c) at the Ce tetrahedral site and (d) on top of an O atom. (e) SFE as a function of chemical potential change for the above-presented models.

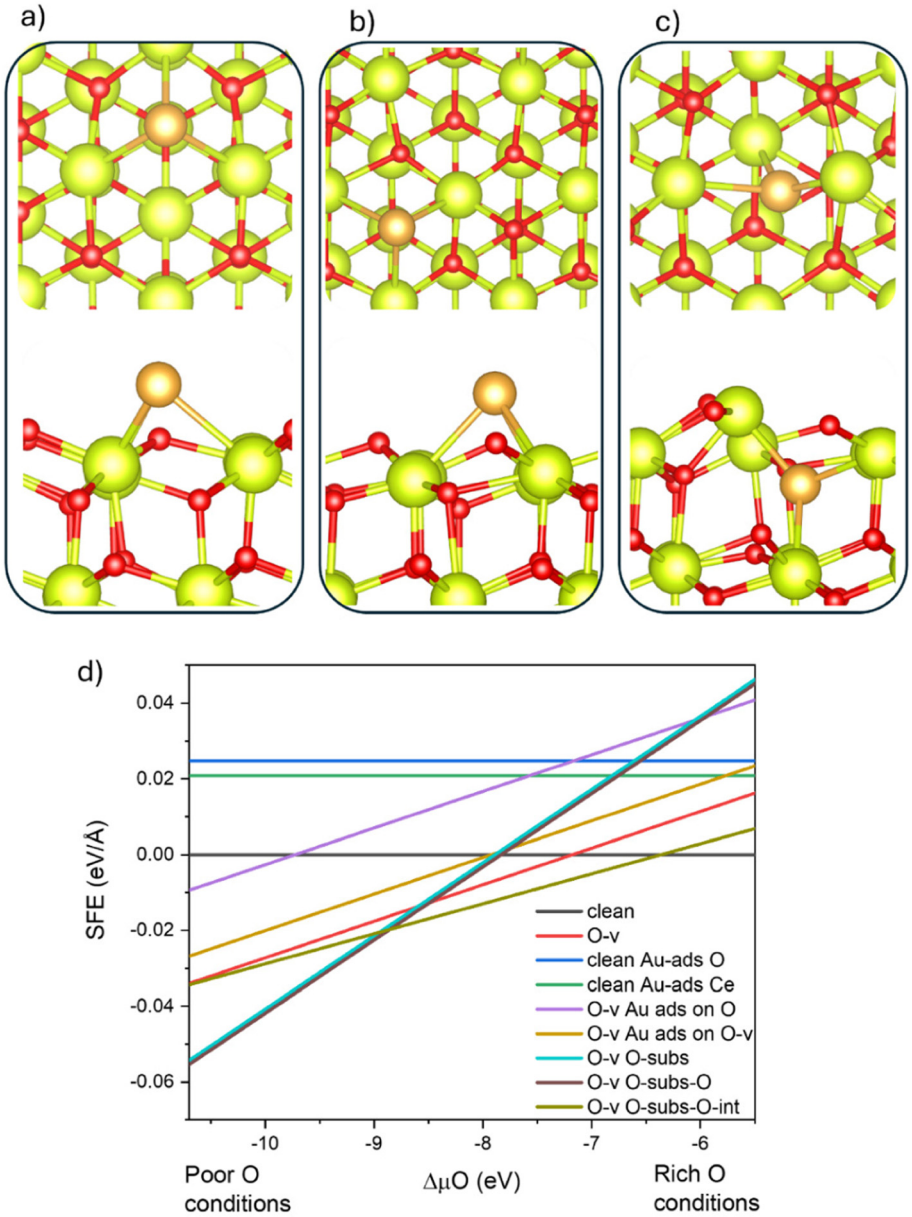

Fig. 6 Adsorption of Au on the CeO_2 (111) surface with an oxygen vacancy defect. (a) Substituting the nearest O to O-v (b) substituting the second nearest O to O-v on top of an O atom, and (c) substituting an O below the O-v. (d) SFE as a function of chemical potential change for the above-presented models.

vacancy does not exhibit an appreciable change. Fig. 6b presents the substitution on the second nearest neighbor O atom, showing structural reconstruction in the vacancy and a small structural shift on the Au atom toward the O-v, likely induced by bond stress. The model in Fig. 6c shows the substitution in the internal O atom closest to the O-v. We observed significant structural deformation induced by the size of the Au atom. All three O-v models with oxygen substitution resulted in increased stability (Fig. 6d) compared to the pristine one and the O-v ones under oxygen-poor conditions, indicating that this type of defect is likely to occur on this surface. In general, the SFE plots for all the assessed models indicated that CeO_2 and Au adsorption on CeO_2 tended to be more stable as the system oxygen defectivity increased. According to the literature, interactions of Au with very electropositive elements induce the formation of the anion behavior of gold,[33–35] which suggests that under-oxidized defective states on CeO_2 could aid the interaction of Au with relatively highly electropositive Ce atoms and induce the anionic behavior of gold. Hence, we proceeded to calculate the Bader charges for all our Au adsorption models to determine the net charge of Au atoms after adsorption. Results are presented in Table 1. They show that for all models with an O-v defect and Au occupying an oxygen site, the net charge of the Au atom was negative, ranging

Table 1 Bader charge analysis for the Au adsorption models

Model	First nearest neighbor atoms	Au net charge (e^-)
Clean Au-ads O	O	−0.09
Clean Au-ads Ce	Ce	+0.32
O-v Au ads on O	O	+0.05
O-v Au ads on O-v	Ce	−0.59
O-v O-subs	Ce	−0.67
O-v O-subs-O-int	Ce	−0.55
O-v O-subs-O-sup	Ce	−0.66

between 0.5 and 0.7 electrons. This indicates that the most stable adsorption models on the CeO_2 (111) surface also exhibited anionic behavior of Au. On the other hand, the non-defective adsorption models presented mostly cationic behavior, as did the de O-v model, where Au adsorbed on top of an O atom, corroborating the observed result that Au occupying oxygen sites tends to exhibit this behavior on this surface. Reports of Bader charge analysis for Au adsorbed on CeO_2 surfaces have also shown negative values for Au.[36] Additionally, the Bader charge for Ce atoms revealed that the nearest neighbors to Au had a net charge of ≈+2 electrons, which, according to the literature, correlates to a Ce^{3+} oxidation state.[37]

Additionally, since the (110) surface has the most negative vacancy formation energy and the observation that anionic behavior gets induced by the presence of oxygen vacancies, we modeled the (110) surface of CeO_2, created surface vacancy models, and adsorbed Au at different surface depths. The results for these relaxed models are presented in Fig. S10, along with their SFE stability plots and Bader charge results. We observed a similar behavior to the (111) surface, where the adsorption of Au substituting an O atom near an O vacancy induced an anionic behavior with a Bader net charge of $-0.71e$ (Fig. S10a), and showed that in deeper surface layers, Au anionic character gradually diminished (Fig. S10b and c), implying that anionic behavior is favored by the surface environment. On the other hand, the SFE plot (Fig. S10d) showed that stability decreased as Au was adsorbed in deep surface layers, implying that the most stable case was the most negative Au charge model too.

To gain further insight into gold charge behavior in different adsorption systems, we performed charge density difference analyses of the CeO_2 (111) Au adsorption models. These results are presented in Fig. S11. Plots depict, in blue iso-surfaces, regions of charge depletion, while in yellow, charge accumulation is shown. Fig. S11a and b correspond to the non-defective adsorption in the tetrahedral site between Ce atoms and on top of O atoms, respectively. Both models show cationic behavior, as evidenced by charge depletion around the Au atoms. On the other hand, in Fig. S10(c–e), models in which Au substitutes for O atoms near an oxygen vacancy are shown, and anionic behavior is observed, as evidenced by a major charge density accumulation around the Au atoms. These results were consistent with Bader charge analysis observations.

As a further validation of the obtained results, we assessed the effect of the slab size on the SFE and the Bader charge of Au, increasing from 3 to 7 Ce atomic layers for a stable anionic behavior Au adsorption model. Results are presented in Fig. S12, showing no significant change in the SFE as well as the Bader charge as the slab size increased, indicating that the employed model size is scalable.

At this point, computational results showed that Au on CeO_2 can behave as an anion. The experimental findings in this regard are presented and discussed in the next section.

Effect of Au concentration on surface chemical composition: tracking Au anionic behavior

An important aspect to consider once we identified the structural conditions that could induce an anionic behavior is that the optimized structural models were developed in a low Au concentration regime. In this context, we expected to identify these chemical species in the low Au concentration regime, yet

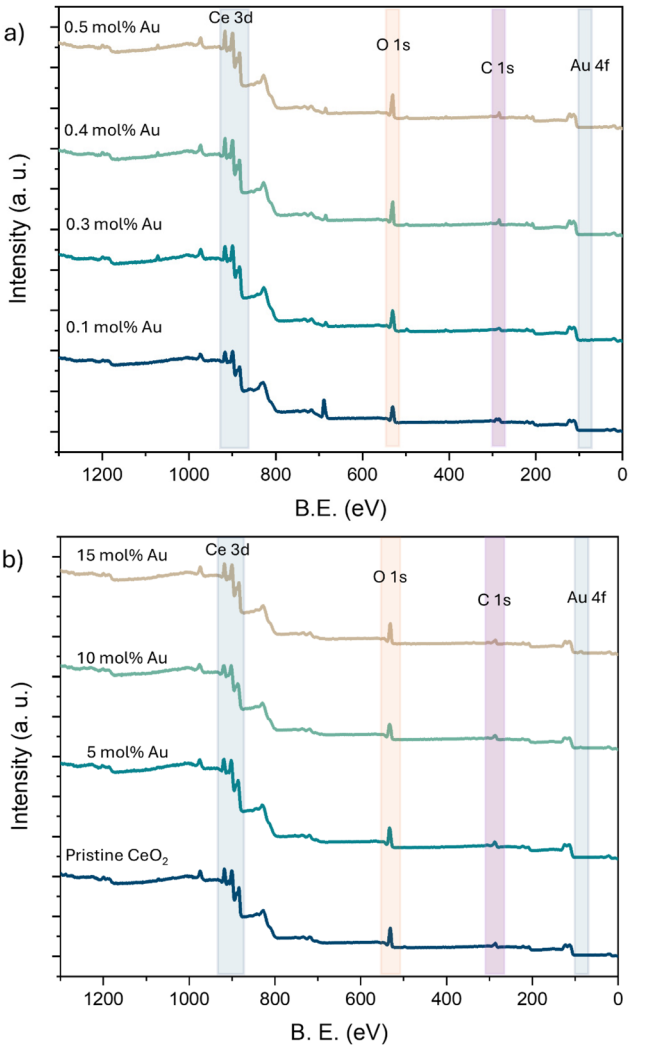

Fig. 7 Survey XPS spectra for the series of samples: (a) at low Au concentrations and (b) at high Au concentrations.

both series of samples were investigated. The chemical analysis was made by XPS. Results for the survey spectra at increasing Au are presented in Fig. 7a for the low concentration regime and Fig. 7b for the high concentration regime. The characteristic peaks for the elements of interest were highlighted: Ce 3d, O 1s, C 1s, and Au 4f. At low concentrations, the peaks in the Au 4f are barely visible. We can see that as the Au concentration increases, the intensity of the small Au 4f peak grows. Ce 3d peaks are clearly visible, as well as the peak for O 1s in both concentration ranges. To establish a relationship between the oxidation state of Ce and the Au concentration, high-resolution spectral windows for Ce 3d, O 1s, C 1s, and Au 4f were also measured. We proceeded to perform the curve fitting for the Ce 3d peaks following the components defined by Romeo and collaborators[38] with modifications as described by Isaacs *et al.*[39] employing the labeling defined in the cited references, identifying the components corresponding to Ce^{3+} and Ce^{4+}. This curve fitting analysis is presented in Fig. 8a for the high concentration regime of samples; the data are shown (after a Shirley background subtraction) as black dots, and the fitted envelope as a purple line. The components corresponding to Ce^{3+} are presented as a beige colored area under the curve, while the Ce^{4+} group is depicted as a blue color palette. XPS atomic percentage quantification was also performed for the high-concentration regime. The results are presented in Fig. 8b as a plot of atomic percentage of the corresponding element as a function of Au concentration in mol%. Results show that with increasing concentrations of Au, the surface amount of Au increased; on the other hand, the O atomic percentage decreased, indicating

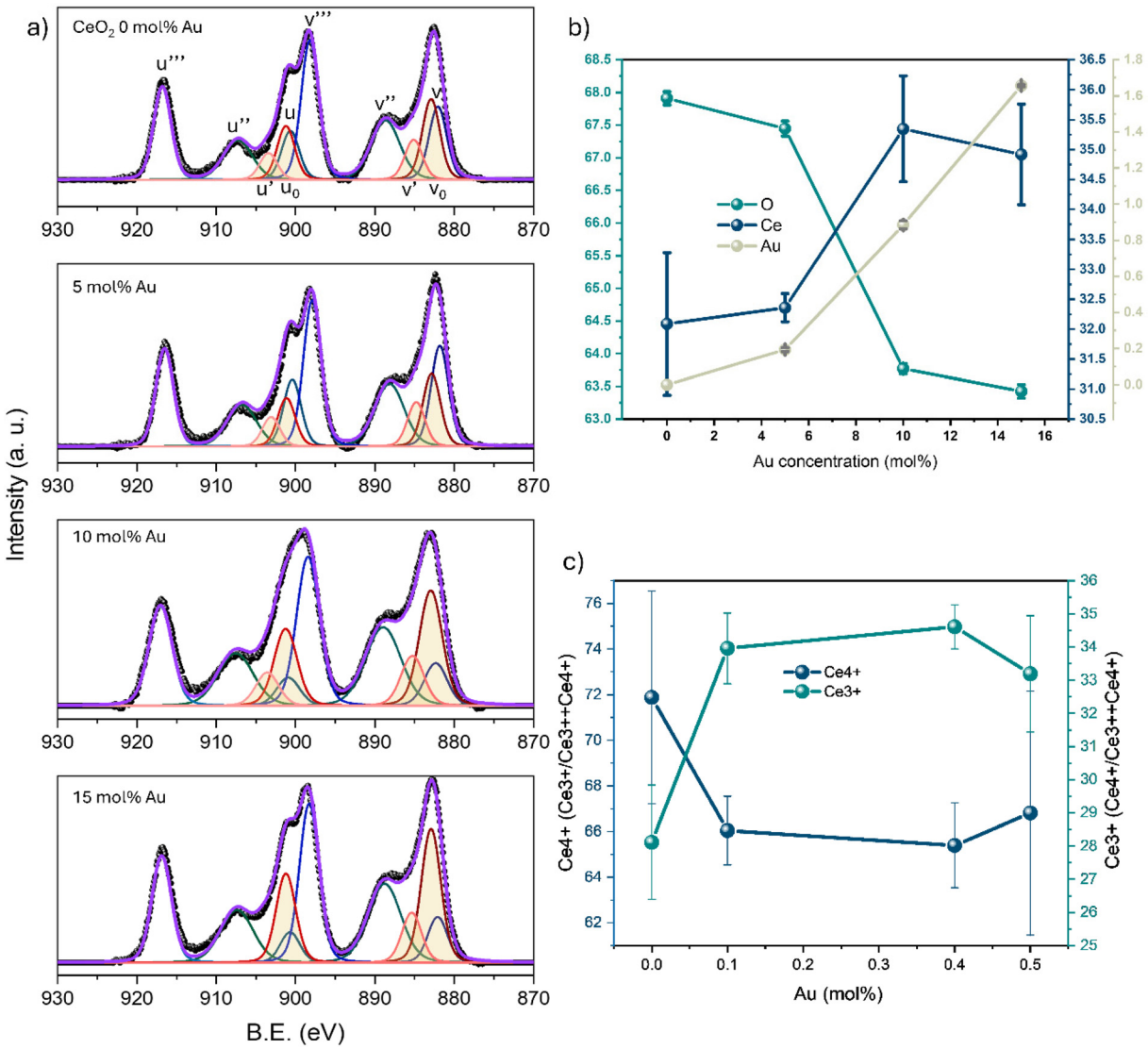

Fig. 8 (a) XPS Ce 3d high-resolution windows (after a Shirley background extraction) for the high Au concentration regime series of samples and the respective components (components were labeled according to literature convention); the envelope is shown in purple and experimental data in black. (b) Surface atomic percentage quantification as a function of Au concentration. (c) Ce^{4+} and Ce^{3+} with respect to the total Ce as a function of Au concentration.

that Au may be substituting oxygen sites. Also, the Ce atomic percentage increased, indicating that the number of defects on CeO_2 also increased. This assertion was confirmed when we constructed a plot of the ratio of each Ce oxidation state relative to the total surface Ce as a function of Au concentration in the low-concentration regime series of samples (Fig. 8c). A direct increase of Ce^{3+} ratio with respect to total Ce is observed, and hence, a diminishing of Ce^{4+} is observed as the Au content rises. This was a clear indication that Au increased the defects and induced a surface reduction effect, also confirming that we had the favorable surface conditions to induce the formation of Au anions, as predicted by DFT simulations. To determine the oxidation state of the Au species, we analyzed the high-resolution windows of the Au 4f XPS spectra for both Au concentration regimes. Curve fitting was performed, and the positions of the modeled components were determined based on position reports for the various gold oxidation states. The spectra for Au 4f after a Shirley background subtraction for the low Au concentration samples are presented in Fig. 9. The results show different oxidation states for gold atoms. The components for Au $4f_{7/2}$ and Au $4f_{5/2}$ for Au^0 are shown in red, Au^{1+} in purple, and Au^{3+} in yellow. Additionally, we found two types of 4f splitting components, which point to the anionic state of Au (Au^{1-}). One with $4f_{7/2}$ at lower binding energy values than Au^0, attributed in the literature to negatively charged Au on the surface of Au particles[14] (shown as green components in Fig. 9); the second negatively charged Au component is attributed to Au atoms substituting oxygen on the surface of the solid; this assignment is consistent with peak appearances reported by Rodriguez and coworkers in XPS studies for CsAu[40] and by Liu and coworkers in their *in situ* XPS study of anionic gold on Au electrodes.[41] Interestingly, the increasing Au amount in the low concentration regime (Fig. 9a–d) shows no identifiable trend in the negatively charged Au species; however, as the concentration increased, the Au^0 relative amount increased. On the other hand, positively charged oxidation states were observed in samples with concentrations of 0.1 mol% and 0.4 mol%, with no particular trend.

Finally, the Au 4f high-resolution window spectra after a Shirley background subtraction for the high Au concentration regime are presented in Fig. 10a. Fitting the component model

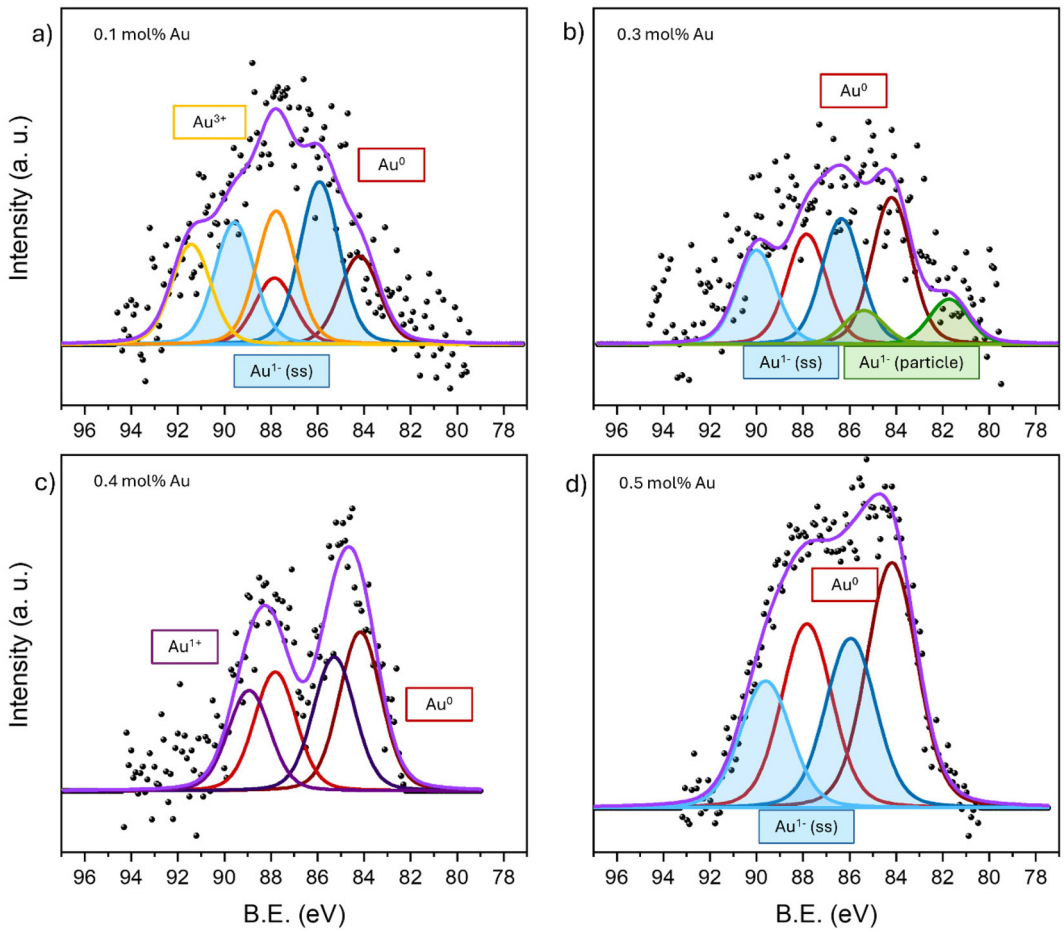

Fig. 9 XPS Au 4f high resolution windows (after a Shirley background extraction) for the CeO_2 modified in the low Au concentration regime: (a) 0.1 mol% Au, (b) 0.3 mol% Au, 0.4 mol% Au and 0.5 mol% Au. Proposed components are shown in colors: Au^0 (red), Au^{1+} (purple), Au^{3+} (yellow), Au^{1-}(ss) (filled blue), and Au^{1-} (particle) (filled green). The experimental result is shown in black, and the envelope is shown in light purple.

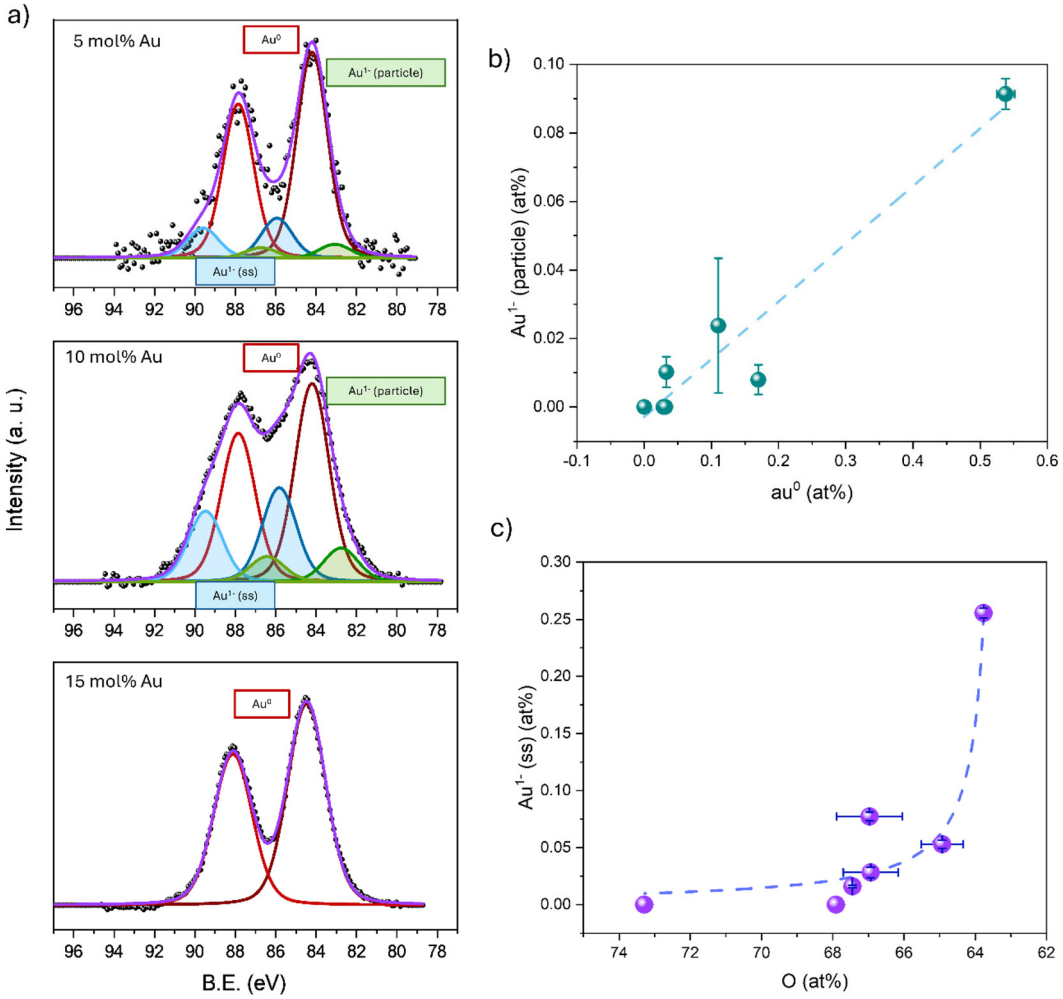

Fig. 10 (a) XPS Au 4f high resolution windows (after a Shirley background extraction) for the CeO_2 modified in the high Au concentration regime. Proposed components are shown in colors: Au^0 (red), Au^{1-}(ss) (filled blue), and Au^{1-} (particle) (filled green). The experimental result is shown in black, and the envelope is shown in light purple. (b) Surface atomic percentage for the Au^{1-} species covering the metallic gold particles (Au^{1-} (particle)) as a function of the atomic percentage for the metallic Au (Au^0) chemical species. (c) Surface atomic percentage for the Au^{1-} species substituting O atoms on the CeO_2 surface (Au^{1-}(ss)) as a function of the surface atomic percentage of O.

shows that metallic (Au^0) species dominated at high concentrations, yet both anionic components appeared even after a 10 mol% addition. However, their relative concentration to the total Au surface amount was higher in low concentration regimes, indicating an effect of concentration on the anionic behavior. This suggests that at lower concentrations, it is more likely for a single O atom to be substituted by Au near an oxygen vacancy, as predicted by our computational simulations. To gain further insight into the structural effects responsible for the observed Au anionic species, we constructed surface atomic percentage (at%) correlation plots. The correlation for the anionic species attributed to the surface of Au particles as a function of the metallic Au (Au^0) concentration is shown in Fig. 10b, indicating that as the amount of Au^0 increases, the Au anionic component on the surface of the metallic Au particles also increases. This result aligns with the component attribution and the literature.[14] On the other hand, Fig. 10c shows the correlation for at% concentration of the Au anionic species attributed to the substitution of oxygen on the solid as a function of the O at%. It is observed that as the oxygen concentration on the surface diminishes, the Au^{1-} concentration increases, in correspondence with the component attribution as well as literature reports.[40,41]

Conclusions

This work presents the synthesis and structural characterization, as well as computational modeling, of Au-doped CeO_2 materials. Results revealed the structural conditions under which the anionic character of gold was observed. Samples were prepared in two Au concentration regimes. Incorporation of Au into the CeO_2 lattice in both concentration regimes was successful as corroborated by XRD and FTIR analyses. An increase in defects and a reductive chemical environment with increasing Au concentration was verified by UV-vis spectra.

The presence of Au loading onto CeO_2 as particles in the high Au concentration samples was identified by SEM images and EDS spectra. The most stable surface models included oxygen vacancies and Au species substituting O atoms near the vacancy site, as revealed by DFT simulation results. Under these conditions, Au behaves as an anion as revealed by Bader charge analysis. Finally, Au occupies O sites, as was confirmed by the XPS analysis, along with further peak modeling and quantification using high-resolution window spectra. On the other hand, different oxidation states of Au were observed, where two sets of components referred to in the literature as Au^{1-} were determined; further quantification correlations confirmed the component assignment, implying that anionic Au species could be inherently present in Au-doped CeO_2 materials. In this sense, this work opens a door to further study catalytic reaction mechanisms. Additionally, it paves the way for future technological applications of anionic gold species in rare-earth oxide materials.

Conflicts of interest

There are no conflicts to declare.

Data availability

The data supporting this article have been included as part of the supplementary information (SI). Supplementary information is available. See DOI: https://doi.org/10.1039/d5nr03470a.

Acknowledgements

We thank DGAPA-UNAM projects IG101124, IN105026 and IA100226 for partial financial support. Calculations were performed in the DGCTIC-UNAM Supercomputing Center projects LANCAD-UNAM-DGTIC-368 and LANCAD-UNAM-DGTIC-422. JGS acknowledges LNS-BUAP project 202201042N and the THUBAT KAAL IPICYT supercomputing center project TKII-JGSA001 for their computational resources. LELG thanks DGAPA-UNAM for the postdoctoral fellowship. The authors acknowledge the technical assistance of David Dominguez, Aldo Rodriguez, Eloisa Aparicio, Israel Gradilla, and Eduardo Murillo.

References

1 M. Rouhani, S. Kord and Z. Mirjafary, *Phys. E*, 2020, **116**, 113710.
2 T. A. Zepeda, R. Ponce-Pérez, A. Solis-Garcia, J. Guerrero-Sanchez, S. Fuentes and S. A. Gomez, *Appl. Catal., B*, 2023, **336**, 122936.
3 Y. Zhao, J. Hu, Z. Tan, T. Liu, W. Zeng, X. Li, C. Huang, S. Wang, Z. Huang and W. Ma, *Sci. Total Environ.*, 2019, **668**, 254–260.
4 Y. Bu, Y. Chen, G. Jiang, X. Hou, S. Li and Z. Zhang, *Appl. Catal., B*, 2020, **260**, 118138.
5 J. L. Vincent and P. A. Crozier, *Nat. Commun.*, 2021, **12**, 5789.
6 A. Trovarelli, C. de Leitenburg and G. Dolcetti, *Catal. Today*, 1999, **50**, 353–367.
7 Z. Li, H. Wang, W. Zhao, X. Xu, Q. Jin, J. Qi, R. Yu and D. Wang, *Catal. Commun.*, 2019, **129**, 105729.
8 F. Bi, X. Zhang, Q. Du, K. Yue, R. Wang, F. Li, N. Liu and Y. Huang, *Mol. Catal.*, 2021, **509**, 111633.
9 G. C. Bond and D. T. Thompson, *Catal. Rev. Sci. Eng.*, 1999, **41**, 319–388.
10 A.-V. Mudring, M. Jansen, J. Daniels, S. Krämer, M. Mehring, J. P. Prates Ramalho, A. H. Romero and M. Parrinello, *Angew. Chem., Int. Ed.*, 2002, **41**, 120–124.
11 A. Pantelouris, G. Küper, J. Homes, C. Feldmann and M. Jansen, *J. Am. Chem. Soc.*, 1995, **117**, 11749–11753.
12 A. M. G. Carranza, R. G. Diaz, D. M. Hoat, J. M. Siqueiros and J. Guerrero-Sanchez, *J. Phys.: Condens. Matter*, 2022, **34**, 235901.
13 P. D. C. Dietzel and M. Jansen, *Chem. Commun.*, 2001, 2208–2209.
14 H. Tsunoyama, N. Ichikuni, H. Sakurai and T. Tsukuda, *J. Am. Chem. Soc.*, 2009, **131**, 7086–7093.
15 M. Mittal, A. Gupta and O. P. Pandey, *Sol. Energy*, 2018, **165**, 206–216.
16 J. Hafner, *J. Comput. Chem.*, 2008, **29**, 2044–2078.
17 G. Kresse and J. Furthmüller, *Phys. Rev. B:Condens. Matter Mater. Phys.*, 1996, **54**, 11169–11186.
18 G. Kresse and J. Furthmüller, *Comput. Mater. Sci.*, 1996, **6**, 15–50.
19 G. Kresse and J. Hafner, *Phys. Rev. B:Condens. Matter Mater. Phys.*, 1993, **47**, 558–561.
20 P. E. Blöchl, *Phys. Rev. B:Condens. Matter Mater. Phys.*, 1994, **50**, 17953–17979.
21 J. P. Perdew, K. Burke and M. Ernzerhof, *Generalized Gradient Approximation Made Simple*, 1996.
22 S. Grimme, J. Antony, S. Ehrlich and H. Krieg, *J. Chem. Phys.*, 2010, **132**, 154104.
23 S. Grimme, S. Ehrlich and L. Goerigk, *J. Comput. Chem.*, 2011, **32**, 1456–1465.
24 S. Li, Y. Li, M. Bäumer and L. V. Moskaleva, *J. Chem. Phys.*, 2020, **153**, 164710.
25 M. Methfessel and A. T. Paxton, *Phys. Rev. B:Condens. Matter Mater. Phys.*, 1989, **40**, 3616–3621.
26 R. Ponce-Pérez, M. T. R. de la Cruz, S. J. Gutiérrez-Ojeda, J. Guerrero-Sánchez, J. Varalda and G. H. Cocoletzi, *Appl. Surf. Sci.*, 2019, **489**, 639–647.
27 K. K. Babitha, A. Sreedevi, P. Priyanka, B. Sabu and T. Varghese, *Structural characterization and optical studies of CeO 2 nanoparticles synthesized by chemical precipitation*, 2015, vol. 53.
28 M. I. Zaki, G. A. M. Hussein, S. A. A. Mansour, H. M. Ismail and G. A. H. Mekhemer, *Colloids Surf., A*, 1997, **127**, 47–56.
29 S. L. Westcott, S. J. Oldenburg, T. R. Lee and N. J. Halas, *Langmuir*, 1998, **14**, 5396–5401.

30 X. S. Huang, H. Sun, L. C. Wang, Y. M. Liu, K. N. Fan and Y. Cao, *Appl. Catal., B*, 2009, **90**, 224–232.
31 M. Nolan, S. Grigoleit, D. C. Sayle, S. C. Parker and G. W. Watson, *Surf. Sci.*, 2005, **576**, 217–229.
32 F. Esch, S. Fabris, L. Zhou, T. Montini, C. Africh, P. Fornasiero, G. Comelli and R. Rosei, *Science*, 2005, **309**, 752–755.
33 M. Jansen, *Chem. Soc. Rev.*, 2008, **37**, 1826–1835.
34 W. Biltz, F. Weibke, V. Hans-Joachim Ehrhorn, R. Wedemeyer and F. Weibke, *Z. Anorg. Allg. Chem.*, 1938, **236**, 12–23.
35 W. E. Spicer, A. H. Sommer and J. G. White, *Phys. Rev.*, 1959, **115**, 57–62.
36 Z. P. Liu, S. J. Jenkins and D. A. King, *Phys. Rev. Lett.*, 2005, **94**, 196102.
37 S. Posysaev, O. Miroshnichenko, M. Alatalo, D. Le and T. S. Rahman, *Comput. Mater. Sci.*, 2019, **161**, 403–414.
38 M. Romeo, K. Bak, J. El Fallah, F. Le Normand and L. Hilaire, *Surf. Interface Anal.*, 1993, **20**, 508–512.
39 M. A. Isaacs, C. Drivas, R. Lee, R. Palgrave, C. M. A. Parlett and D. J. Morgan, *Appl. Surf. Sci. Adv.*, 2023, **18**, 100469.
40 J. A. Rodriguez, J. Hrbek, M. Kuhn and T. K. Sham, *J. Vac. Sci. Technol., A*, 1993, **11**, 2029–2033.
41 Z. Liu, O. Höfft, A. S. Gödde and F. Endres, *J. Phys. Chem. C*, 2021, **125**, 26793–26800.